LAWRENCE
LIVERMORE
NATIONAL
LABORATORY

LLNL-JRNL-421320

UEDGE Simulation of Edge Plasmas in DIII-D Double Null Configurations

G. D. Porter, T. W. Petrie, T. D. Rognlien, M. E. Rensink

December 11, 2009

Physics of Plasmas

Disclaimer

UEDGE simulation of edge plasmas in DIII-D double null configurations

G. D. Porter, T. W. Petrie, T. D. Rognlien, M. E. Rensink

ABSTRACT—Analysis of plasma flow in the edge of double null hybrid mode DIII-D plasmas is reported. The 2D fluid plasma code UEDGE is used for the analysis. The effect of impurity radiation from intrinsic carbon sputtered from plasma facing surfaces is included as is the effect of plasma drifts. Two discharges in which the flux surfaces through the poloidal field nulls (X-points) are separated by 1 cm at the outer midplane are analyzed. The discharges differ only in the direction of the ion ∇B drift. It is shown that the flow of both primary ions and intrinsic impurities are dominated by the effect of plasma drifts. Variations in the recycling of deuterium ions, as seen in D_α emission profiles, are qualitatively consistent with experiment and are driven by the effect of ExB drifts associated with radial gradients of the electron temperature at the secondary separatrix. Trace argon impurity is introduced to simulate the transport of argon used in the experiment to enhance divertor radiation power. Penetration of the trace argon to the closed field lines depends on the direction of the ion ∇B drift, consistent with experiment. The analysis described here includes the effect of a deuterium gas puff to establish the "puff and pump" configuration. The poloidal flow of impurities is a balance between the projection of the parallel flow and poloidal drifts, primarily from ExB. It is shown that the effect of the gas puff is primarily to alter the electron temperature profile and thus affects impurity flow via alteration of ExB drifts, not via entrainment in deuterium ion parallel flow.

1 INTRODUCTION

Understanding the physics of the edge plasma of a diverted tokamak is important for development of future magnetic confinement fusion devices. Interaction of the power and particle exhaust with plasma facing material walls yields sources of fuel neutrals and sputtered impurities. Control of these recycling neutrals and impurities is crucial to the successful operation of the confined plasma. Operation of plasmas in advanced tokamak modes[1] places even greater stresses on plasma facing components since the edge temperatures are higher and densities lower leading to more intense power loads on these components. It is envisioned that the power loads will be ameliorated in part by enhancing radiation losses through injection of impurity gasses in the divertor regions. It will be crucial that the transport of the injected impurities is controlled to prevent dilution of the confined plasma and thus diminution of the fusion power. Such control requires an understanding of the physics of plasma flow in the edge plasma. An examination of this physics in double null configurations is begun here with analysis of DIII-D advanced plasma operation using the UEDGE fluid plasma code[2].

Magnetic configurations referred to here as "double null" (DN) are characterized by

having two poloidal field nulls (X-points) that are important for the description of the geometry of the edge plasma. The two X-points lie on the same magnetic flux surface for a balanced double null configuration and on slightly different flux surfaces for an unbalanced double null configuration. We describe simulation of unbalanced DN DIII-D plasmas here. Simulation of balanced DN plasmas is in progress and will be the subject of a later paper. We describe simulations of two unbalanced DN discharges with the distance between the flux surfaces which pass through the two X-points about 1 cm at the low (magnetic) field side (LFS) midplane. The X-point which lies between the closed field lines and field lines which strike the plasma facing surfaces (the dominant X-point) lies at the top of the DIII-D vessel. We consider discharges in which the ion ∇B drift is downward ($v_{\nabla B} \downarrow$), away from the dominant X-point (forward field), and upward ($v_{\nabla B} \uparrow$), toward the dominant X-point (reversed field).

The experimental results obtained in DN discharges on DIII-D are summarized briefly in Section 2. The UEDGE simulations of these discharges are described in Section 3. The transport of trace argon impurities introduced into these simulations and the experiment is described in Section 4 and we conclude with a summary in Section 5.

2 UNBALANCED DN DISCHARGE DESCRIPTION

The DIII-D team has performed several experimental campaigns over the last few years to assess fuel particle exhaust and impurity particle transport into the core confined plasma. [3-7] These experimental campaigns have been primarily aimed at understanding fuel and impurity transport in H-mode operation with particular attention to plasma operation in hybrid mode. The experimental results indicate that the most important factors in determining transport of fuel and impurities are a combination of the direction of the ion ∇B drift velocity and how close the plasma equilibrium is to a balanced double null. Two unbalanced DN discharges have been selected for UEDGE analysis in this paper, shots 125850 and 126894. The magnetic configuration of these discharges differ only in the direction of the toroidal magnetic field. The magnetic reconstruction of discharge 125850 is shown in Figure 1. The toroidal magnetic field of this discharge is in the "forward" direction, meaning that the ion ∇B drift direction is downward ($v_{\nabla B} \downarrow$). The flux surface corresponding to the last closed flux surface, the primary separatrix, has been emphasized in this figure. The secondary separatrix is defined by the flux surface that passes through the lower X-point. The separation between these two flux surfaces is 1 cm at the outer midplane. The shape of the magnetic flux surfaces of the second discharge, 126894, is identical to that shown in Figure 1 but the toroidal magnetic field is in the "reversed" direction so the ion ∇B drift is upward ($v_{\nabla B} \uparrow$), toward the dominant X-point.

Both of these discharges are run with a plasma current of 1.2 MA and toroidal magnetic field of 2 T on axis (edge q of 4.1). The plasma is operated in the hybrid mode with neutral beam heating power of about 5 MW. Additional deuterium gas (about 1000 atom Amp) is injected into the scrape-off layer (SOL) 2 s into the

discharge to operate in the "puff and pump" mode. This mode is an attempt to entrain impurities in the enhanced deuterium ion flow toward the plates and thus restrict the flow of impurities from the divertor region. The poloidal location of the deuterium gas puff is shown in blue. Argon neutrals are injected in the upper PF region to enhance radiation in the primary divertor region and thus reduce divertor heating. Three cryopumps–one in the upper inner PF region; one under the upper outer baffle; and one under the lower outer baffle–are cooled to exhaust both deuterium and argon.

3 UNBALANCED DN UEDGE RESULTS

The UEDGE[2] code has been used to simulate the two discharges described in the previous section. This 2D fluid plasma model has been compared in detail with experimental results on the DIII-D device previously.[8, 9] Most of the earlier simulations have been restricted to single null configurations in which the second X-point is located on a flux surface far from the dominant X-point. The existence of a secondary X-point can therefore be ignored and the problem treated as a single null configuration. Rensink reported simulations of configurations with two X-points previously.[10, 11] His early DN simulations showed the importance of plasma drifts in determining divertor power and particle loads, but were restricted to geometries in which the divertor plates were assumed orthogonal to the poloidal flux surfaces. In contrast the simulations reported here use a divertor geometry that approximates that of the experiment. In addition a more realistic fluid neutral model that includes the inertial response of deuterium neutrals[12] is used here and the effect of impurity radiation from carbon impurities introduced by physical and chemical sputtering of plasma facing surfaces is included. The drift effects included in the UEDGE model include the Pfirsch-Schlüter drifts described by Chankin.[13] The consistency of the UEDGE model with that of Chankin has been confirmed for simple L-mode lower single null plasmas. This paper emphasizes the effect of drifts in the divertor regions and hence does not focus on these Pfirsch-Schlüter drifts. The shape of the mesh used for simulation of discharge 125894 ($v_{\nabla B} \uparrow$, toward the dominant X-point) is shown in Figure 2. The details of the mesh in the region near both X-points are shown. The flux surfaces corresponding to the two X-points are shown in magenta. The mesh near the midplane of the device is not shown to enable better visualization of the divertor regions. The detailed shape of the upper dome is not reproduced in the divertor plate definition used for the HFS of the upper divertor, as seen in Figure 2 to avoid extremely distorted meshes which are numerically difficult. The mesh extends from the closed flux surface corresponding to a normalized poloidal flux of Ψ_N=0.9 outward to the SOL flux surface which is first limited by the walls of the device, i.e. Ψ_N=1.12. Note that the flux surfaces on the LFS terminate on the angled top of the upper pumping baffle, that is the top of the upper baffle is treated as a divertor plate in the simulation. The magnetic configuration of discharge 125850 ($v_{\nabla B} \downarrow$) is very similar to that of 126894. The UEDGE mesh for this shot is not shown since it is similar to that shown in Figure 2. The mesh for both discharges is based on flux surfaces from the EFIT[14] magnetic reconstructions for each shot and therefore are not identical, but represent the experiment accurately.

The following assumptions and boundary conditions have been used for the base case solutions:

- The effect of all plasma ExB, ∇B and curvature drifts is included[15, 16].

- Intrinsic carbon impurities are included assuming the source is chemical and physical sputtering from plasma facing surfaces. Carbon neutral atoms and all carbon ionization states are included. Sputtering yields found in the literature are used.[17, 18]

- The deuterium ion density on the innermost flux surface (Ψ_N=0.9) is specified consistent with TS data. The density is assumed constant on this surface.

- The radial power flowing in both the ion and electron channels on the innermost flux surface is specified to be 2.45 MW for discharge 125850 and 2.30 MW for discharge 126894. The total power for both shots corresponds to that inferred from the experiment.

- A fluid neutral model, including ion/neutral parallel momentum exchange[12], is used to determine the spatial variation of deuterium neutrals. The neutral diffusion is assumed to be pressure driven.

- The deuterium neutral density on the innermost flux surface is specified to be 2.0×10^{13} m^{-3}. This density is low enough that the simulations are not sensitive to the boundary condition.

- The radial density and temperature scale lengths on the outermost and private flux region (PF) surfaces are assumed to be 10 cm.

- The deuterium ion flux to all surfaces is recycled as deuterium neutral atoms with a recycling coefficient of 1.0. The carbon ion flux to all surfaces is not recycled, i.e. the recycling coefficient is set to 0.

- All plasma facing surfaces are assumed to pump part of the incident neutral deuterium flux. The neutral albedo, equivalent to pumping rate, is specified separately on the divertor plates, the outermost flux surface and the PF surfaces. The assumed albedos are described below. The carbon neutral flux is assumed to recycle, as will be discussed subsequently.

- The electron and ion thermal cross field transport is assumed to be diffusive with spatially constant diffusivity, as is the cross field momentum transport. The particle transport is also assumed to be diffusive with a poloidally constant diffusion coefficient. The particle diffusion coefficient is varied radially to enable better simulation of the upstream electron density profile measured with the Thomson Scattering (TS) system. The particle diffusivity is assumed to be the same for all ion species.

- A steady state neutral deuterium gas puff of 800 atom Amps is introduced in a position corresponding to the gas puff used in the experiments (just below

the upper, outer pumping baffle). Simulations with and without this gas puff are compared.

The albedo of the neutral deuterium flux to plasma facing surfaces is specified to simulate the pumping geometry suggested by the experimental team, viz. there is no neutral pumping on the inner lower plate, 2% of the neutral thermal particle flux to the inner upper plate is pumped, 10% of the neutral flux to both outer plates is pumped; 2% of the neutrals striking both the upper and lower private flux (PF) surfaces are pumped. The pumping assumed on the outermost flux surface is different for the $v_{\nabla B}\downarrow$ and $v_{\nabla B}\uparrow$ simulations because of difficulty with convergence. We assume 3% of the neutral flux to the HFS of the outermost flux surface is pumped and 2% of the neutral flux to the LFS for the $v_{\nabla B}\downarrow$ field case. We assume 2% of the neutral flux to the HFS and 5% of the flux to the LFS is pumped for the $v_{\nabla B}\uparrow$ case. The assumption of a fixed radial density scale length at the outermost flux surface yields a finite ion flux to the outermost flux surface. This ion flux is recycled as neutral atoms with a recycling coefficient of 1.0. The same assumption is made on the private flux (PF) surfaces.

The dominant sputtering mechanism for carbon sources is chemical sputtering. Carbon is generated as a hydrocarbon with this sputtering mechanism. Hydrocarbons are not pumped efficiently by carbon walls; hence we assume the carbon neutral atoms recycle from all plasma facing surfaces with an albedo of 1.0. UEDGE simulations in which the assumption of recycling for the carbon neutrals are characterized by having a total impurity radiated power much less than measured experimentally. Hence it is assumed that carbon neutrals are recycled.

The particle diffusivity near the separatrix is reduced to better match the radial plasma density profile measured by the Thomson Scattering (TS) system. The combination of the wall pumping and particle transport models yields a finite ion flux from the core into the simulation domain. This ion flux is equal to the total particle removal rate, permitting a steady state solution.

3.1 Simulations with and without a gas puff

The initial steady state UEDGE simulations obtained with the boundary conditions and assumptions listed above are described here. The simulated plasma profiles at the top of the plasma and R=1.94 m, i.e. the position of the Thomson scattering measurement shown in Figure 1, is compared with the TS measurements in Figure 3. The electron temperature profile for both directions of the toroidal field is well represented with simulations using a simple spatially constant electron thermal diffusivity (0.4 m^2/s for $v_{\nabla B}\downarrow$ field direction and 0.15 m^2/s for $v_{\nabla B}\uparrow$).

The measured density profiles, however, are more poorly fit by the simulations. The density profile is determined by a combination of the assumed cross field transport model, and the assumptions of the neutral pumping by the plasma facing components. Neither the transport model nor the characteristics of the walls are well

known experimentally. It is assumed that one could improve the agreement between the measured and simulated density profiles by arbitrarily varying the transport and pumping model. However, it is not at all clear that such a solution would be unique and therefore not helpful for understanding the physics of plasma operation. Rather, we assume that the simulated density profile is "close enough" to the measured to enable extraction of understanding of the plasma flows in the edge and SOL plasmas. Note, however, that the particle diffusivity is assumed to be reduced near the separatrix, i.e. a transport barrier for particle transport exists. This assumption is made to avoid SOL densities that are much larger than seen experimentally.

Consider first the poloidal variation of the electron temperature shown in Figure 4. The color scale used in this figure is logarithmic, and has been chosen to permit examination of the variation of the temperature profile in the SOL. The temperature on the closed field lines rises from the last closed flux surface to the innermost surface considered in the simulation, as seen in Figure 3, but this variation is masked in Figure 4 by the expanded color scale, i.e. the colors are saturated inside the magnetic separatrix. The variations in electron temperature are important in assessing the origin of ExB drifts that are instrumental in determining plasma flows in the SOL. There is a large radial variation in the electron temperature near the secondary separatrix in the upper, inner divertor region, particularly for the $v_{\nabla B} \uparrow$ simulation. This variation leads to a radial electric field that produces an ExB drift that pulls ions away from the inner divertor for the $v_{\nabla B} \uparrow$ configuration, and pushes the ions toward the inner divertor for $v_{\nabla B} \downarrow$. These drifts will be important in understanding the characteristics of the D_α emission considered subsequently. The electron temperature just above the outer baffle top is reduced for $v_{\nabla B} \downarrow$ case, leading to a poloidal electric field that pulls ions radially away from the outer strike point, a flow that is visible in the D_α emission in this region. Note also that the plasma on the lower inner divertor is essentially detached, with an electron temperature less than 1 eV, for the $v_{\nabla B} \downarrow$ simulation. The electron temperature in the far SOL of the HFS is substantially lower for the $v_{\nabla B} \uparrow$ configuration. The low temperature is important for understanding the re-ionization of recycling deuterium neutrals as well as the flow of injected argon impurities. These variations in the electron temperature will be apparent in the line emission profile of primary neutrals as well as both intrinsic (carbon) and injected impurities. There is experimental data for the D_α emission in the divertor regions of the discharges simulated here, but none for impurity emission.

Knowledge of the poloidal variation of the electron temperature is valuable in understanding plasma flow, but is typically only determined experimentally at one or two poloidal locations. Many experiments rely on spectroscopic measurements of line emission of both deuterium and impurities to determine poloidal variation of plasma parameters. Experimentally some of the profiles of visible line emission are available using the tangentially viewing TV cameras on DIII-D.[19] The simulation results can be compared qualitatively with experiment using these line emission profiles. The D_α emission in the upper divertor obtained in the simulations described here are shown in Figure 5. The emission profiles obtained in simulations with and without the gas puff are shown for comparison. The color scale used in this figure is logarithmic

and is the same for all four images. The affect of the deuterium gas puff can be inferred by comparing the upper panels with the lower. The D_α emission on the LFS of the upper divertor region extends further downward with the gas puff. The neutral gas introduced along the outermost flux surface, about 15 cm below the top of the upper baffle is ionized producing higher deuterium emission. Note that the D_α emission on the HFS of the upper divertor is also intensified when gas is puffed on the LFS for the $v_{\nabla B} \uparrow$ case (compare the two right panels of Figure 5). The bright emission along the secondary separatrix (magenta dashed line) is a direct result of the effect of the ExB drift. The electron temperature decreases significantly across this secondary separatrix leading to a radial electric field, as shown in Figure 4. This electric field yields a poloidal plasma drift that is away from the plate for $v_{\nabla B} \uparrow$, and toward the plate for $v_{\nabla B} \downarrow$. Ions created by ionization of recycling deuterium neutrals on the HFS of the upper divertor are thus pulled away from the plate when the ∇B drift is up leading to higher density and hence brighter emission along the secondary separatrix. In contrast the ions created by ionization of the recycling neutrals are pushed toward the plate when the ion ∇B drift is down forcing the density on the plate to be high, and hence D_α emission closer to the inner plate. A similar effect is created on the LFS except in this case the bright finger of D_α emission appears for $v_{\nabla B} \downarrow$. The emission maximum does not follow the flux surfaces as closely on the LFS because there is a significant poloidal electric field as well as a radial field, leading to a combination of poloidal and radial plasma drift. These effects are visible in the experiment as well.

The dynamic range of the tangential TV data on DIII-D does not permit comparison of the emission profile with simulation results that span five orders of magnitude as shown in Figure 5. The D_α emission profiles obtained in simulations with an 800 A gas puff is compared with experimentally obtained profiles using a linear color scale in Figure 6. The upper limit of the color scale for the $v_{\nabla B} \downarrow$ (forward field) shot is 1.5×10^{22} photons/s/m^3, and the $v_{\nabla B} \uparrow$ (reversed field) shot is 2.8×10^{22} photons/s/m^3 for the experimental data. The simulated and measured D_α emission brightness agree within a factor of two to three. The agreement between experiment and simulation is consistent within the uncertainty of the absolute calibration of the experimental data.

The broad D_α emission profile on the LFS of the $v_{\nabla B} \downarrow$ shot and the HFS of the $v_{\nabla B} \uparrow$ shot are qualitatively consistent in the simulated and measured profiles. These features can be attributed to the effect of ExB drifts. Hence the experimental data qualitatively supports the contention that these drifts play an important role in plasma flow in the active divertor region.

The simulated D_α emission in the secondary, i.e. lower, divertor is less consistent with that seen experimentally as shown in Figure 7. The simulations yield higher emission on the LFS of the lower divertor, as seen experimentally. However, the simulation shows significant emission on the HFS for the $v_{\nabla B} \downarrow$, which is not seen experimentally. The HFS emission in the lower divertor was reduced somewhat in a simulation in which the cross field transport coefficients were assumed to vary as $1/B_T$ (more

"ballooning-like", i.e., peaking at the outer unstable region of the flux surface) rather than constant. However, the reduction in the HFS emission was not sufficient to bring the simulation into agreement with the data. The discrepancy in the emission in the secondary divertor is not understood but may arise from the nature of plasma detachment. We noted earlier that the plasma in the lower inner divertor region was detached with an electron temperature less than 1 eV for the $v_{\nabla B}\downarrow$ simulation (see Figure 4). The D_α emission in this region is therefore dominated by emission arising from three body recombination. The intensity of this line emission is very sensitive to electron temperature. Small variations in the electron temperature in this region could lead to very large (orders of magnitude) variations in D_α emission. Hence the disparity between simulated and measured emission in this region may arise because of small variations in the electron temperature between experiment and simulation.

3.2 Analysis of poloidal flows

One of the primary purposes of the experiments discussed here was to establish poloidal flows by puffing and pumping deuterium gas and thereby confine impurity gases in the divertor region through entrainment in the parallel flow of the primary ions.[20] One measure of the poloidal flow is the ion flux to the divertor plates. The plate flux into each of the four divertors for the $v_{\nabla B}\downarrow$ simulation with and without a gas puff is shown in Figure 8. The ion fluxes normal to the divertor plates are plotted, not normal to the magnetic field line. The sign convention for the ion flux is that a flow in the clockwise direction is positive. Thus flow out of the lower inner and upper outer divertor plates is positive as is flow into the upper inner and lower outer plates. The abscissa for each plot is the distance of the flux surface from the primary separatrix at the outer midplane. The same scale is used for the ion flux for each of the four divertor plates. Note that the standard UEDGE sign convention means an ion flux into the lower inner and upper outer divertor is negative, that into the upper inner and lower outer is positive, i.e., all currents are into the plates. The ion flux to the primary divertor, the upper, exceeds that to the lower divertor. Furthermore, the ion flux to the lower divertor exists primarily outside the secondary separatrix, i.e. ions that diffuse radially across the primary separatrix are mainly deposited in the upper divertor. The peak of the ion flux on the upper inner divertor lies outside the primary strike point about 2.5 cm at the plate (about 0.5 cm at the LFS midplane). This shift is a direct result of the radial ExB drift from the poloidal electric field created by the drop in the electron pressure between the X-point and the divertor plate. This radial shift will vary if one is successful in enhancing radiation power losses by injecting impurities. Thus if the radiation loss is enhanced there should be an increased poloidal electron pressure gradient along the upper inner separatrix producing a larger radial shift in the peak particle flux. It may therefore be necessary to make small adjustments in the strike point location to optimize pumping.

The addition of an 800 A puff of neutrals near the top of the upper outer baffle produces a small increase in the plate ion flux to both the inner and outer upper divertor plates. The increased ion flux, and the concomitant increase in recycling

neutrals reduces the poloidal electric field on the upper inner divertor yielding a peak ion flux which lies closer to the strike point.

The ion plate fluxes for the simulation of the $v_{\nabla B}\uparrow$ discharge with and without a gas puff are shown in Figure 9. There is a larger in/out asymmetry in the ion flux to the upper divertor for this field direction. Furthermore the ion flux peak in the upper inner divertor is not shifted radially but is near the strike point. Note, however, that there is more ion flux to the PF region of the upper inner divertor when the toroidal field is reversed. This increase in the PF ion flux is probably due to the radial shift we described for the $v_{\nabla B}\downarrow$ case. The peak ion flux to the upper outer divertor is about 10% higher than for the $v_{\nabla B}\downarrow$ case and is shifted radially outward. The ion flux to the lower outer divertor is somewhat higher and is more tightly peaked near the strike point of the secondary separatrix than for the $v_{\nabla B}\downarrow$ case. This may lead to more efficient pumping by the lower cryopump.

The divertor ion fluxes are a fundamental measure of the plasma flow in the SOL. The simulated fluxes to all four plates with and without a gas puff are shown in Figure 8 and Figure 9. The simulated plate fluxes obtained with 800 A gas injection are compared with Langmuir probe measurements in the upper divertor in Figure 10. The divertor ion flux data is plotted against the normalized poloidal flux to enable direct comparison of the flux on the inner and outer divertors at the same flux surface. The primary separatrix lies at Ψ_n=1.0. The probe data is in agreement with simulation for the $v_{\nabla B}\downarrow$ case (shot 125850) both on the inner and outer divertor plates. It is not possible to determine whether the outward shift of the peak of the ion flux to the inner divertor is seen in the experiment since there is data from only one probe. Although the magnitude of the simulated flux to the outer divertor of the $v_{\nabla B}\uparrow$ case is consistent with the probe data, the simulation shows an outward shift of the peak that is not seen in the data. This discrepancy may arise because of the plate definition used in the simulation. The UEDGE mesh extends slightly under the pumping baffle as seen in Figure 2. The simulated ion flux peaks at the poloidal flux corresponding to the secondary separatrix, i.e. at the corner of the mesh on the upper outer divertor. The peak ion flux is therefore created at a point where the neutrals recycling from the divertor plate are emitted toward the separatrix, leading to an enhancement in the flux. However, this effective corner is not present in the experiment since neutrals recycling off the floor are directed downward, into the pumping baffle.

Note especially that the ion flux to the PF portion of the upper plate is much higher for the $v_{\nabla B}\uparrow$ case than for the $v_{\nabla B}\downarrow$ case (see Figure 8 and Figure 9). The radial flux across the separatrix along the upper outer leg (from the HFS of the upper X-point to the upper outer strike point) is –58 A for the $v_{\nabla B}\downarrow$ case with 800 A gas puff (TPfdn15) and –682 A for the $v_{\nabla B}\uparrow$ case (TPgdn13). (A negative flux across this surface is from the SOL to the PF region.) This radial flux is predominately near the plate and is dominated by the ExB drift flux due to the poloidal electric field. One would expect the poloidal electric field near the strike point to be independent of the direction of the toroidal field, leading to a reversal of the ExB radial flow when the field is reversed. However, the poloidal electric field near the outer strike point reverses

when the toroidal field is reversed due to the radial shift of the plasma. In other words, when the toroidal field is reversed the poloidal electric field near the upper outer plate shifts the plasma outward (see Figure 8 and Figure 9). This plasma shift modifies the structure of the poloidal electric field leading to an enhancement of the radial ion flux into the PF region and hence an enhancement of the parallel ion flux to the plate in the PF region. As noted before, this outward plasma shift near the upper outer strike point is not seen in the probe data, and the enhanced ion flux in the PF region is also not seen on the single probe in that region. This suggests that the approximations made for generation of the UEDGE mesh near the input to the pumping baffle are not sufficient to accurately simulate all details of the plasma near that baffle. However, the similarity of the simulated and measured upstream plasma profiles, together with the qualitative agreement of the divertor D_α emission profiles and the agreement in the magnitude of the simulated and measured divertor ion fluxes suggests the simulations are relevant to understanding SOL flows in this configuration.

A gas puff will be effective in entraining impurities in the divertor region only if it creates a flow and only if the poloidal flow of the impurity is dominated by the projection of parallel flow, not by the effect of drifts. If parallel flow dominates the poloidal flow of impurities, entrainment by deuterium flow will be dominant only if the parallel drag force exceeds other parallel forces such as the ion temperature gradient flow.[21] The components of the poloidal flux of total carbon for the $v_{\nabla B} \downarrow$, no gas puff case is shown at four poloidal positions in Figure 11. The sign convention for the poloidal flux is that a clockwise flux is positive. Hence flux going from the lower, inner divertor to the upper inner divertor is positive, as is flux from the upper outer divertor to the lower outer divertor. The contribution of the ion ∇B drift to the poloidal flux is insignificant at all poloidal locations and is shown in green in Figure 11. The total carbon poloidal flux in the SOL, shown in red, is in general a balance between the flux due to the ExB flow (shown in blue), and the projection of the parallel flow (shown in cyan). The exception is at the lower outer divertor where the poloidal carbon flux in the SOL is dominated by the flux from the ExB drift near the strike point of the secondary separatrix. In all cases the poloidal flux from plasma drifts is important. This raises the question of the effectiveness of a deuterium gas puff in entraining impurities.

The effect of an 800 A neutral deuterium gas puff on the poloidal carbon flux for the forward field case is shown in Figure 12. It was shown previously that the deuterium puff had only a small effect on the deuterium flux to the divertor plates (see Figure 8). Comparison of Figure 12 with Figure 11 indicates there is little effect of the deuterium puff on the impurity flow as well, but it is interessting to note how the puff affects the impurity flow. Consider first the outer SOL region on the LFS since the gas puff is located in this region near the upper divertor. The net carbon flux (red curve) goes from slightly negative (upward) at the LFS midplane to slightly positive (downward) in the far SOL ($R-R_{sep} > 0.02$). This change is predominately due to a change in the radial electric field and hence a change in the ExB carbon flux. There is also an increase in the net carbon flux just below the lower LFS X-point. This increase arises from both an increase in the ExB flux and an increase in the parallel flux. The parallel carbon flux is determined by a variety of processes including the

parallel ion temperature gradient, cross field transport and sputtering sources on the plasma facing surfaces. The dominant source of carbon in the region under consideration is cross field transport across the secondary separatrix. The parallel flux shown in Figure 11 and Figure 12 is therefore transporting carbon which arises in other regions of the plasma. The net carbon flux on the LFS in the region between the primary and secondary separatrices is upward at the outer midplane and is reduced by the introduction of the gas puff. The net carbon flux in this region is a balance between the ExB flux associated with the radial electric field and the parallel flux. Note that in the absence of the ExB flux the net carbon flux at the midplane would be downward rather than upward. The carbon flux below the secondary X-point is dominated by the ExB flux and is relatively insensitive to the gas puff at the top of the vessel. Consider next the HFS of the SOL. The net carbon flux outside the secondary separatrix at the inner plasma midplane remains upward when gas is puffed into the LFS plasma, and increases significantly. This is primarily from an increase in the parallel carbon flux. Note that there is no connection between these field lines and the lines onto which the deuterium gas is puffed. Hence the increased carbon flux due to the gas puff arises from plasma changes in other regions, in particular a reduction in the electron temperature in the lower inner divertor and a concomitant increase in the neutral carbon penetration from sputtering sources. Note that the gas puff leads to a reduction of the net carbon flux in the region between the primary and secondary separatrices on the upper HFS divertor. This reduction arises in spite of the fact that the gas puff increased the deuterium flow to the upper inner divertor as noted in Figure 8. The modification of the ExB drift flux by the deuterium gas puff plays a significant role in the net carbon flux throughout the SOL. The introduction of the gas puff is not simply a technique which enhances the deuterium parallel flux and entrains carbon. Rather enhanced recycling caused by the extra gas modifies the electron temperature profile, and hence modifies the flux of carbon driven by electric field drifts.

The previous conclusion that the plasma drifts play an important role in the poloidal impurity transport was based only on the simulations of the $v_{\nabla B}\downarrow$. Since the plasma drifts reverse when the toroidal field is reversed, the poloidal flow of impurities should change significantly when the field is reversed. The poloidal carbon ion fluxes for the $v_{\nabla B}\uparrow$, no gas puff case is shown in Figure 13. The effect of reversing the toroidal field can be inferred by comparing this figure with Figure 11. The largest effect is on the poloidal flux on the closed field lines. These variations may well be important for understanding the H-mode physics of the pedestal region. However, this paper is focused on flow in the SOL so we will leave the discussion of the physics of the pedestal for the future. The net carbon flux in the SOL is strongly modified by reversing the toroidal field. The SOL fluxes with the field reversed are influenced by the flux from plasma drifts, as was found for simulation of the $v_{\nabla B}\downarrow$ shot. The drift fluxes reverse when the toroidal field is reversed, as expected. The poloidal carbon fluxes for the $v_{\nabla B}\uparrow$ case with 800 A gas puff are not shown in the interest of space. Suffice it to say the results are similar to those obtained for the $v_{\nabla B}\downarrow$ case. The effect of a deuterium gas puff on the poloidal flow of impurities is through variation in the electric fields in the SOL as well as variations in the parallel flow through drag with the hydrogen species and modification of carbon sources arising from changes in

the SOL plasma associated with increased recycling.

4 FLOW OF ARGON INTRODUCED IN PF

Argon was injected into the upper private flux region of the discharges simulated in this report. We examine the flow of argon in the UEDGE simulations by introducing a small (0.1 atom Amp) argon neutral puff into the upper inner private flux. The UEDGE code is capable of solving for the self-consistent density of all ion species, deuterium, carbon and argon. However, the problem becomes impractical with that many species, i.e. the code requires a large memory and the run time is very long. To avoid these difficulties we have frozen the deuterium and carbon densities to those obtained without argon injection and treat this problem as trace argon injection. The objective is to examine the argon transport in the self-consistent plasma obtained without argon injection. The argon radial transport coefficient is assumed to be identical to that used for both deuterium and carbon.

One way of determining the effect of the direction of the toroidal field on argon transport is to examine the total argon density (summed over all ionization states). The total argon density obtained for the $v_{\nabla B}\downarrow$ and $v_{\nabla B}\uparrow$ geometries is shown in Figure 14. The argon density on the closed field lines is about twenty times larger for $v_{\nabla B}\uparrow$ than $v_{\nabla B}\downarrow$. The experiment resulted in a factor of three increase for $v_{\nabla B}\uparrow$. Thus the UEDGE simulations are qualitatively consistent with experiment, but not quantitatively. The lack of quantitative agreement may be a result of ignoring the effect of argon radiation on the background plasma in the simulations. One can examine the source of higher argon density on the closed lines for $v_{\nabla B}\uparrow$. The net argon ion flux across the separatrix is very small for both configurations. In general the net ion flux seen on the HFS of the separatrix is balanced by the net ion flux on the LFS leading to the small total argon ion flux. There is no net fueling of the core by radial transport of the argon ions for either field configuration. About 1% of the injected argon neutral flux (1 mA) flows across the separatrix just below the upper inner X-point for $v_{\nabla B}\uparrow$ case. The total neutral flux across the separatrix is about three orders of magnitude less for the $v_{\nabla B}\downarrow$ case. The injected neutral argon is ionized easily in the PF region and is swept to the outer divertor for $v_{\nabla B}\downarrow$ by the ExB drifts in the PF region and to the inner divertor for $v_{\nabla B}\uparrow$. The argon ions are then recycled as neutral argon at each of the divertor plates. The pumping efficiency of the inner upper pump is much less than that of the outer upper pump so the argon neutrals arising from recycling of the argon ions at the divertor are more efficiently pumped with $v_{\nabla B}\downarrow$. Furthermore the electron temperature on the HFS SOL is lower for the $v_{\nabla B}\uparrow$ case yielding a longer mean free path for argon neutrals (see Figure 4). The combination of these effects produce a higher neutral argon flux across the separatrix for $v_{\nabla B}\uparrow$ and hence higher argon ion density on the closed lines when the neutrals finally ionize.

5 SUMMARY AND CONCLUSIONS

The flow of fuel and impurity particles in the scrape-off layer of double null tokamak configurations has been examined in this paper. The fluid plasma code UEDGE has been used to simulate DIII-D hybrid mode plasmas. It has been shown that plasma drift effects, particularly ExB drifts, play an important role in the transport of intrinsic carbon impurities and argon impurities introduced to enhance radiated power in the divertor region. Deuterium neutrals introduced to establish a "puff and pump" geometry to restrict argon neutrals to the divertor region act to modify the SOL electron temperature profile, and hence control the electric fields which drive impurity transport via plasma drifts. The direction of the toroidal magnetic field, i.e. the direction of the ion ∇B drift, plays a crucial role in determining the flow of argon neutrals to the closed field lines. When argon ions are swept to the HFS region of the dominant divertor by ExB plasma drifts neutral argon resulting from recycling of the argon ion flow to the divertor plate is able to penetrate to the closed lines because of lower electron temperatures on the HFS as well as less efficient pumping. This combination of effects leads to a factor of three increase in argon density on the closed lines in the experiment and a factor of twenty increase in the simulations discussed here. The flow of impurities in the divertor regions of DN plasma is determined by the in/out asymmetries of the divertor plasma. This asymmetry is in turn determined in large part by the plasma drifts.

6 REFERENCES

[1] C. M. Greenfield, J. C. DeBoo, T. C. Luce, et al., Physics of Plasmas **7**, 1959 (2000).

[2] T. Rognlien, J. Milovich, M. Rensink, et al., J. Nucl. Mater. **196-198**, 347 (1992).

[3] T. W. Petrie, S. L. Allen, N. H. Brooks, et al., Nuclear Fusion **46**

, 57 (2006).

[4] T. W. Petrie, N. H. Brooks, M. E. Fenstermacher, et al., Nuclear Fusion **48** (2008).

[5] T. W. Petrie, D. Buchenauer, D. N. Hill, et al., J. Nuc. Mater. **196-198**, 848 (1992).

[6] T. W. Petrie, C. M. Greenfield, R. J. Grobener, et al., Journal of Nuclear Materials **290**, 935 (2001).

[7] T. W. Petrie, N. H. Brooks, M. E. Fenstermacher, et al., Submitted to Nuclear Fusion (2009).

[8] G. D. Porter, M. Fenstermacher, R. Groebner, et al., Contrib. Plasma Phys. **34**,

454 (1994).

[9] G. D. Porter, R. Isler, J. Boedo, et al., Phys. Plasma **7**, 3663 (2000).

[10] M. E. Rensink, S. L. Allen, G. D. Porter, et al., Contributions to Plasma Physics **40**, 302 (2000).

[11] M. E. Rensink, C. J. Lasnier, T. W. Petrie, et al., Contrib. Plasma Phys. **42**, 181 (2002).

[12] F. Wising, D. A. Knoll, S. I. Krasheninnikov, et al., Contrib. Plasma Phys. **35**, 136 (1996).

[13] A. V. Chankin, N. Asakura, G. Corrigan, S. K. Erents, W. Fundamenski, H. W. Muller, R. A. Pitts, P. C. Stangeby, Nuclear Fusion **47**, 762 (2007).

[14] L. L. Lao, H. S. John, R. D. Stambaugh, et al., Nucl. Fusion **25**, 1611 (1985).

[15] T. D. Rognlien, G. D. Porter, and D. D. Ryutov, J. Nucl. Mat. **266-269**, 654 (1999).

[16] T. D. Rognlien, D. D. Ryutov, N. Mattor, et al., Phys plasma **6**, 1851 (1999).

[17] J. W. Davis and A. A. Haasz, J. Nucl. Mat. **241-243**, 37 (1997).

[18] W. Eckstein, J. Nucl. Mat. **248** (1997).

[19] M. E. Fenstermacher, S. L. Allen, D. N. Hill, et al., Contrib. Plasma Phys. **36**, 127 (1996).

[20] M. J. Schaffer, D. G.Whyte, N. H. Brooks, et al., Nucl. Fus. **35**, 1000 (1995).

[21] J. Neuhauser, W. Schneider, R. Wunderlich, et al., Nuclear Fusion **24**, 39 (1984).

Figure captions

Figure 1 Magnetic reconstruction of DIII-D discharge 125850. The primary separatrix has been emphasized.

Figure 2 UEDGE mesh used for simulation of the DIII-D discharge 126894.

Figure 3 Comparison of experimentally measured upstream plasma profiles with UEDGE simulation. The forward field discharge (125850, $v_{\nabla B}\downarrow$) is shown on the left and the reversed field discharge (126894, $v_{\nabla B}\uparrow$) on the right.

Figure 4 Poloidal variation on the electron temperature profile for the forward (left, $v_{\nabla B}\downarrow$) and reversed (right, $v_{\nabla B}\uparrow$) field simulations.

Figure 5 Comparison of D_α emission profiles in the upper divertor for simulations of the forward (left panels, $v_{\nabla B}\downarrow$) and reversed field (right panels, $v_{\nabla B}\uparrow$) discharges with 0 A gas puff (top panels) and 800 A gas puff (bottom panels).

Figure 6 Comparison of D_α emission for forward (left, $v_{\nabla B}\downarrow$) and reversed (right, $v_{\nabla B}\uparrow$) field simulations with 800 A gas puff using a linear color scale.

Figure 7 Comparison of the simulated and measured D_α emission profiles in the lower divertor region for the forward (left, $v_{\nabla B}\downarrow$) and reversed (right, $v_{\nabla B}\uparrow$) field discharges.

Figure 8 Deuterium ion flux to plates for $v_{\nabla B}\downarrow$ simulations (discharge 125850)

Figure 9 Deuterium ion flux to plates for $v_{\nabla B}\uparrow$ simulations (discharge 126894)

Figure 10 Comparison of simulated upper divertor ion fluxes with Langmuir Probe data for the forward ($v_{\nabla B}\downarrow$) and reversed ($v_{\nabla B}\uparrow$) field discharges.

Figure 11 Components of total carbon ion poloidal flux for the $v_{\nabla B}\downarrow$, no gas puff simulation.

Figure 12 Components of total carbon ion poloidal flux for the $v_{\nabla B}\downarrow$, 800 A gas puff simulation.

Figure 13 Poloidal variation of the components of the total carbon poloidal flux for the $v_{\nabla B}\uparrow$, no gas puff simulation.

Figure 14 Distribution of total argon density for the forward (left, $v_{\nabla B}\downarrow$) and reversed (right, $v_{\nabla B}\uparrow$) simulations.

This work performed under the auspices of the U.S. Department of Energy by Lawrence Livermore National Laboratory under Contract DE-AC52-07NA27344.

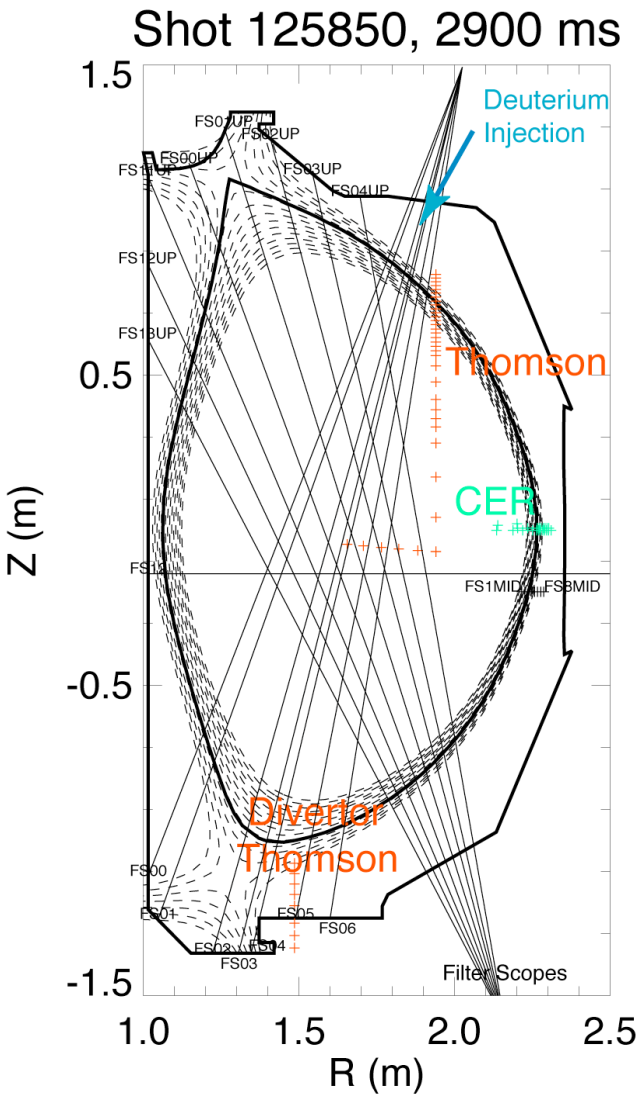
Shot 125850, 2900 ms
Deuterium
Injection
Thomson
CER
Divertor
Thomson
Filter Scopes
FS02UP
FS00UP
FS03UP
FS04UP
FS12UP
FS13UP
FS1MID
FS3MID
FS00
FS01
FS02
FS03
FS04
FS05
FS06
1.5
0.5
-0.5
-1.5
Z (m)
1.0
1.5
2.0
2.5
R (m)

Fig 1

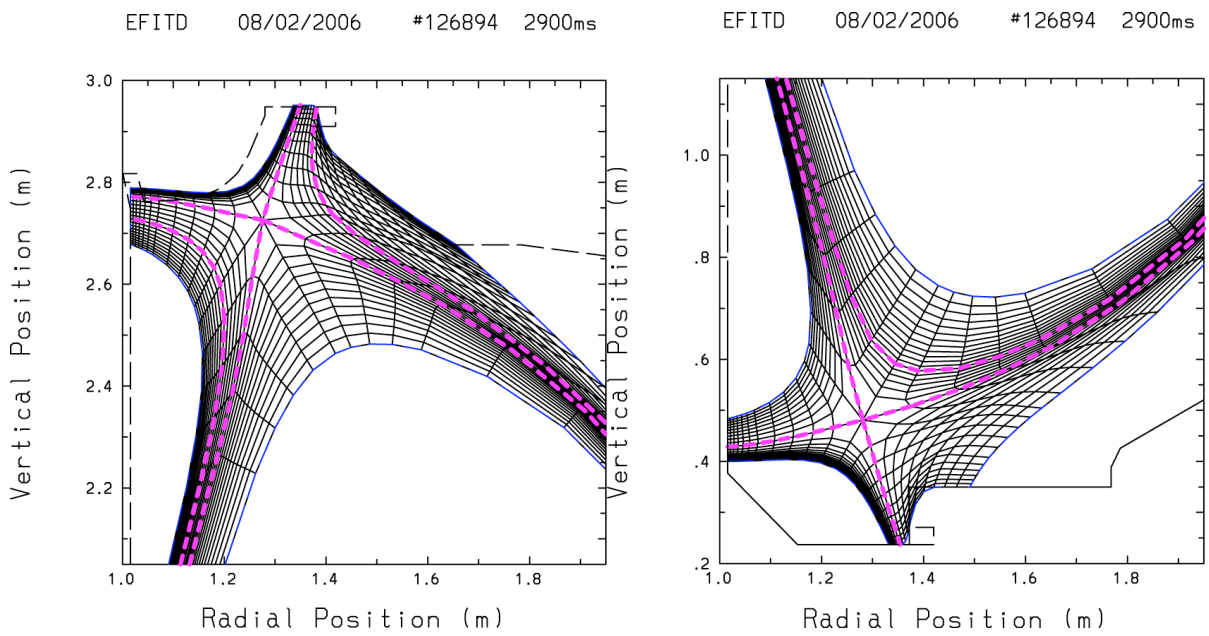
EFITD 08/02/2006 #126894 2900ms
Vertical Position (m)
Radial Position (m)
EFITD 08/02/2006 #126894 2900ms
Vertical Position (m)
Radial Position (m)

Fig. 2

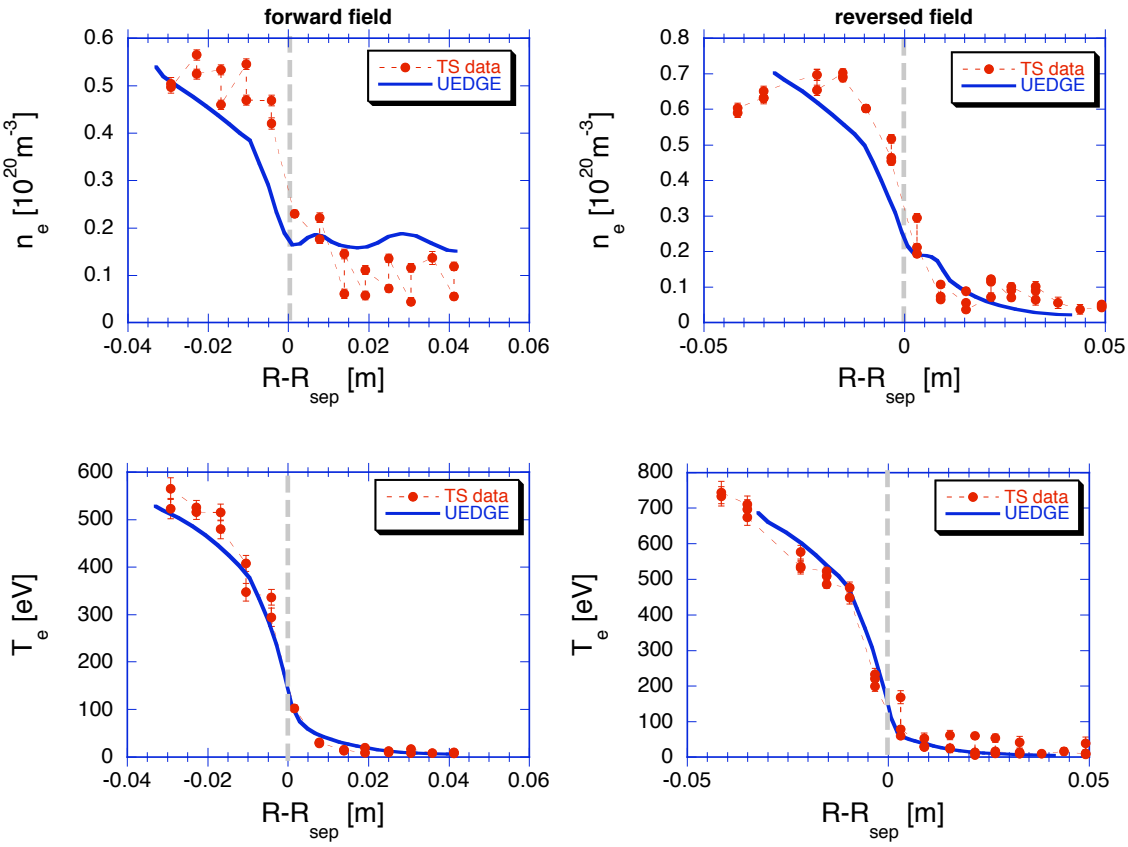
forward field
reversed field
TS data
UEDGE
n_e [10^20 m^-3]
T_e [eV]
R-R_sep [m]

Fig 3

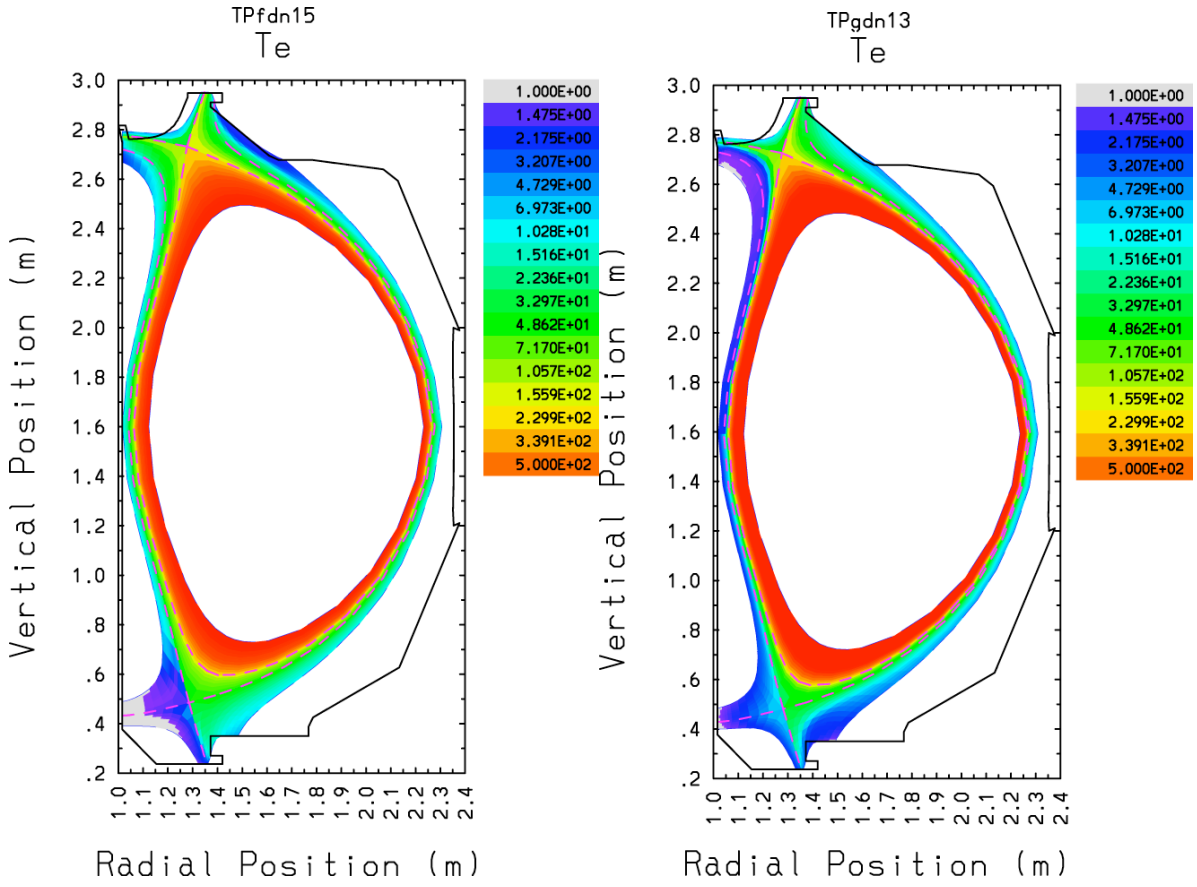
TPfdn15
Te
Vertical Position (m)
Radial Position (m)
1.000E+00
1.475E+00
2.175E+00
3.207E+00
4.729E+00
6.973E+00
1.028E+01
1.516E+01
2.236E+01
3.297E+01
4.862E+01
7.170E+01
1.057E+02
1.559E+02
2.299E+02
3.391E+02
5.000E+02
TPgdn13
Te
Vertical Position (m)
Radial Position (m)

Fig. 4

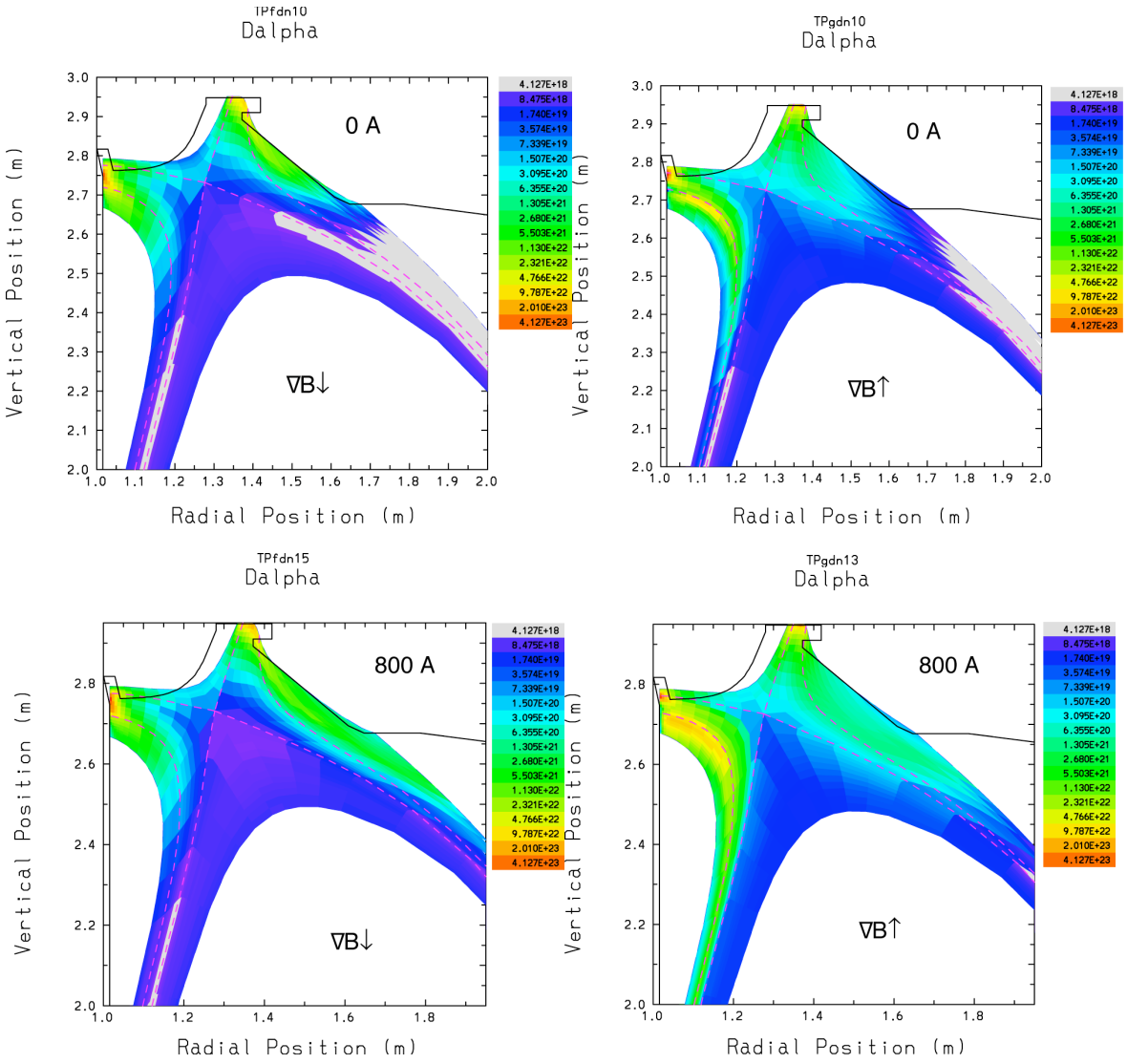
TPfdn10
Dalpha
0 A
∇B↓
TPgdn10
Dalpha
0 A
∇B↑
TPfdn15
Dalpha
800 A
∇B↓
TPgdn13
Dalpha
800 A
∇B↑
Vertical Position (m)
Radial Position (m)
4.127E+18
8.475E+18
1.740E+19
3.574E+19
7.339E+19
1.507E+20
3.095E+20
6.355E+20
1.305E+21
2.680E+21
5.503E+21
1.130E+22
2.321E+22
4.766E+22
9.787E+22
2.010E+23
4.127E+23

Fig 5

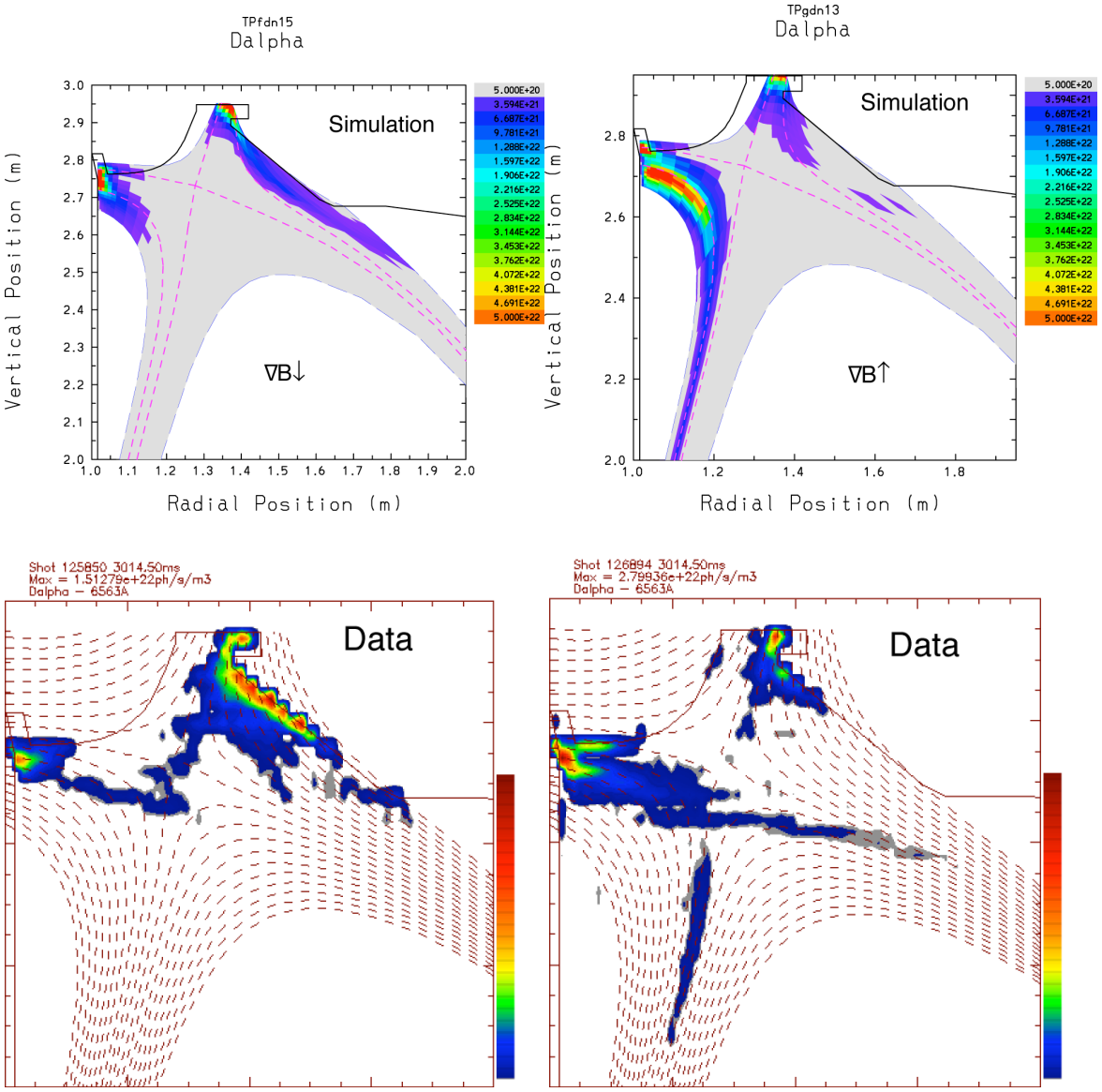
TPfdn15
Dalpha
Simulation
∇B↓
Vertical Position (m)
Radial Position (m)
TPgdn13
Dalpha
Simulation
∇B↑
Vertical Position (m)
Radial Position (m)
Shot 125850 3014.50ms
Max = 1.51279e+22ph/s/m3
Dalpha – 6563A
Data
Shot 126894 3014.50ms
Max = 2.79936e+22ph/s/m3
Dalpha – 6563A
Data

Fig 6

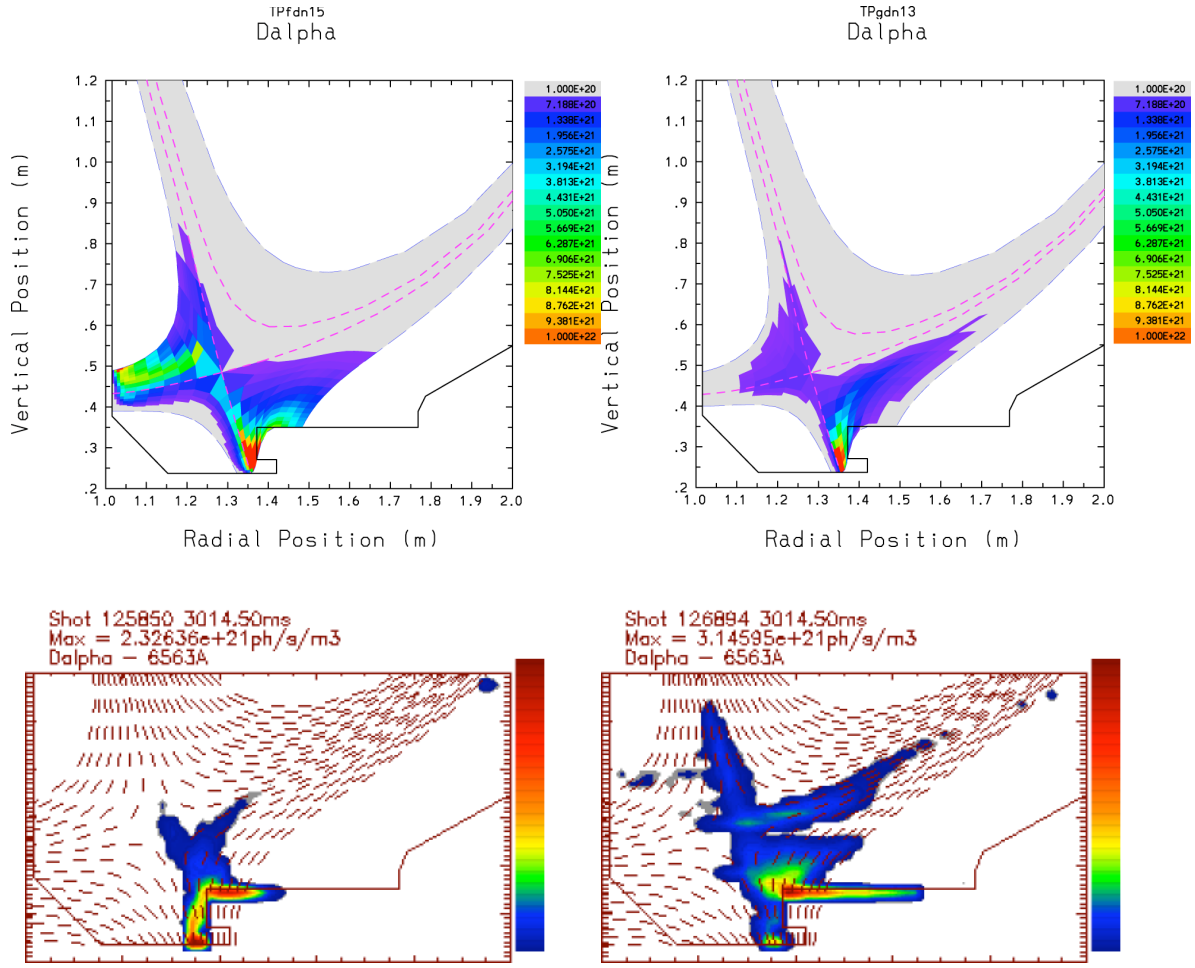
TPfdn15
Dalpha
Vertical Position (m)
Radial Position (m)
1.000E+20
7.188E+20
1.338E+21
1.956E+21
2.575E+21
3.194E+21
3.813E+21
4.431E+21
5.050E+21
5.669E+21
6.287E+21
6.906E+21
7.525E+21
8.144E+21
8.762E+21
9.381E+21
1.000E+22
TPgdn13
Dalpha
Vertical Position (m)
Radial Position (m)
Shot 125850 3014.50ms
Max = 2.32636e+21ph/s/m3
Dalpha – 6563A
Shot 126894 3014.50ms
Max = 3.14595e+21ph/s/m3
Dalpha – 6563A

Fig 7.

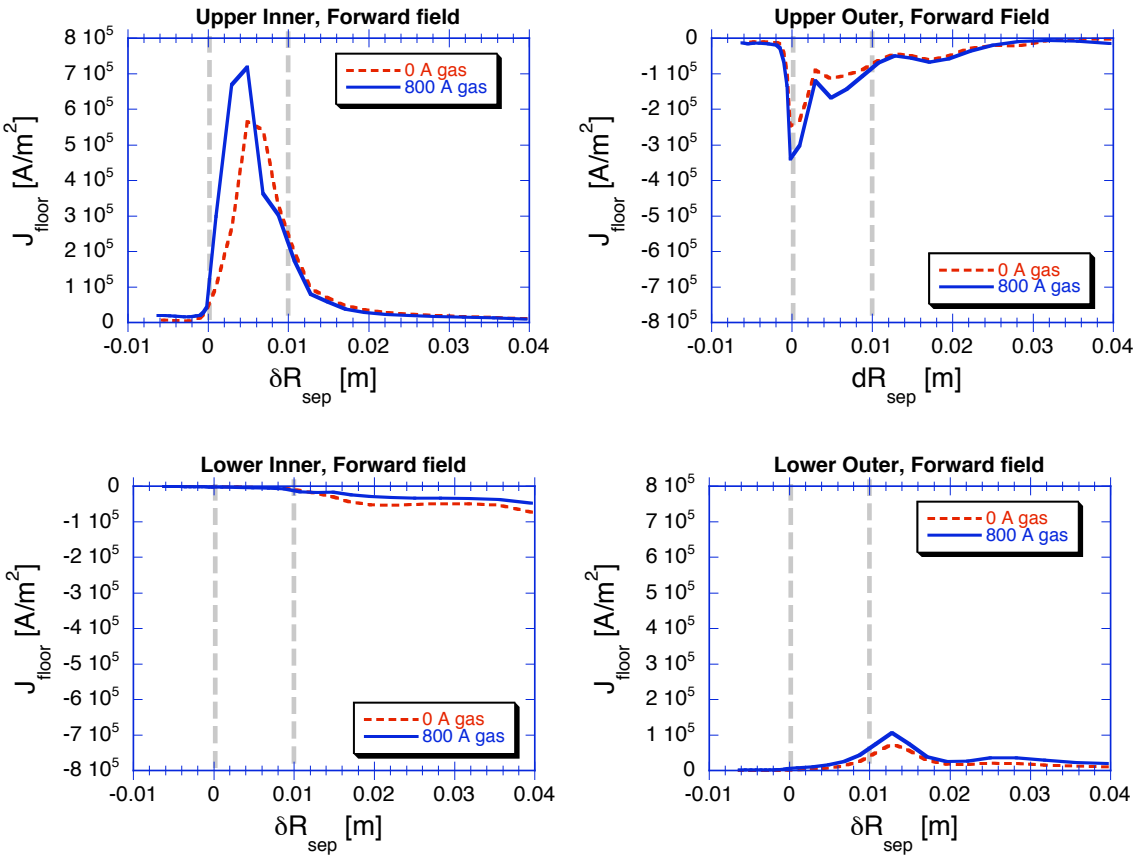
Upper Inner, Forward field
Upper Outer, Forward Field
Lower Inner, Forward field
Lower Outer, Forward field
0 A gas
800 A gas
J_floor [A/m^2]
δR_sep [m]
dR_sep [m]

Fig. 8

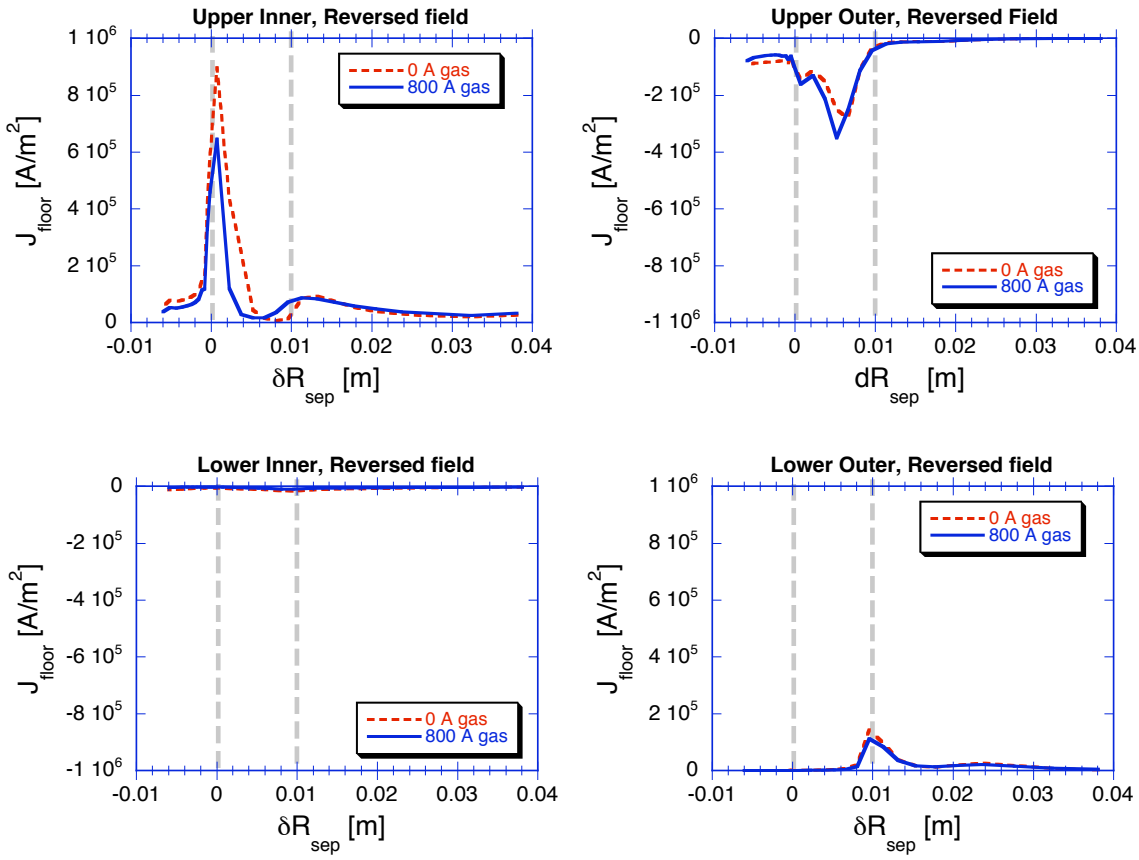
Upper Inner, Reversed field
Upper Outer, Reversed Field
Lower Inner, Reversed field
Lower Outer, Reversed field
0 A gas
800 A gas
J_floor [A/m^2]
δR_sep [m]
dR_sep [m]

Fig 9.

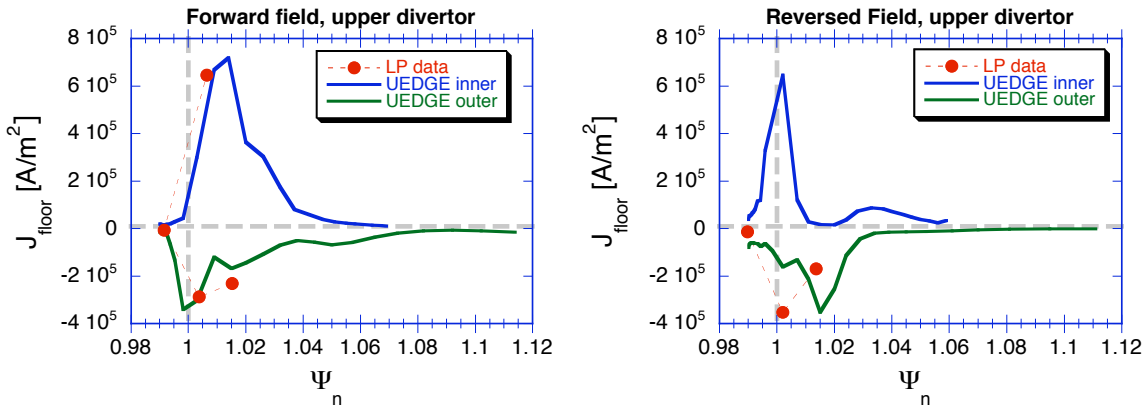
Forward field, upper divertor
Reversed Field, upper divertor
LP data
UEDGE inner
UEDGE outer
J_floor [A/m^2]
Ψ_n
8 10^5
6 10^5
4 10^5
2 10^5
0
-2 10^5
-4 10^5
0.98
1
1.02
1.04
1.06
1.08
1.1
1.12

Fig 10

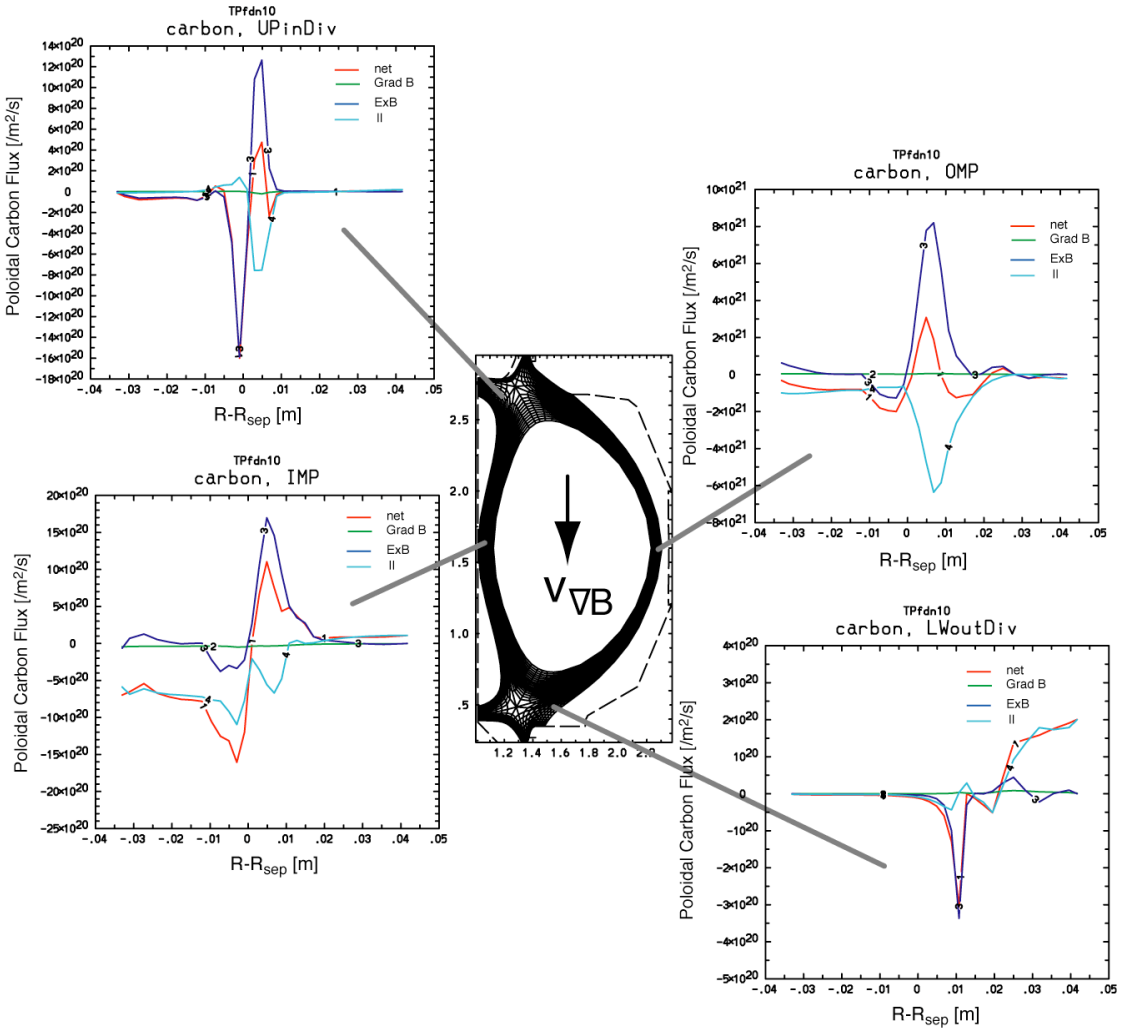
TPfdn10
carbon, UPinDiv
net
Grad B
ExB
⊥
Poloidal Carbon Flux [/m²/s]
R-Rsep [m]
TPfdn10
carbon, OMP
TPfdn10
carbon, IMP
TPfdn10
carbon, LWoutDiv
V∇B

Fig 11

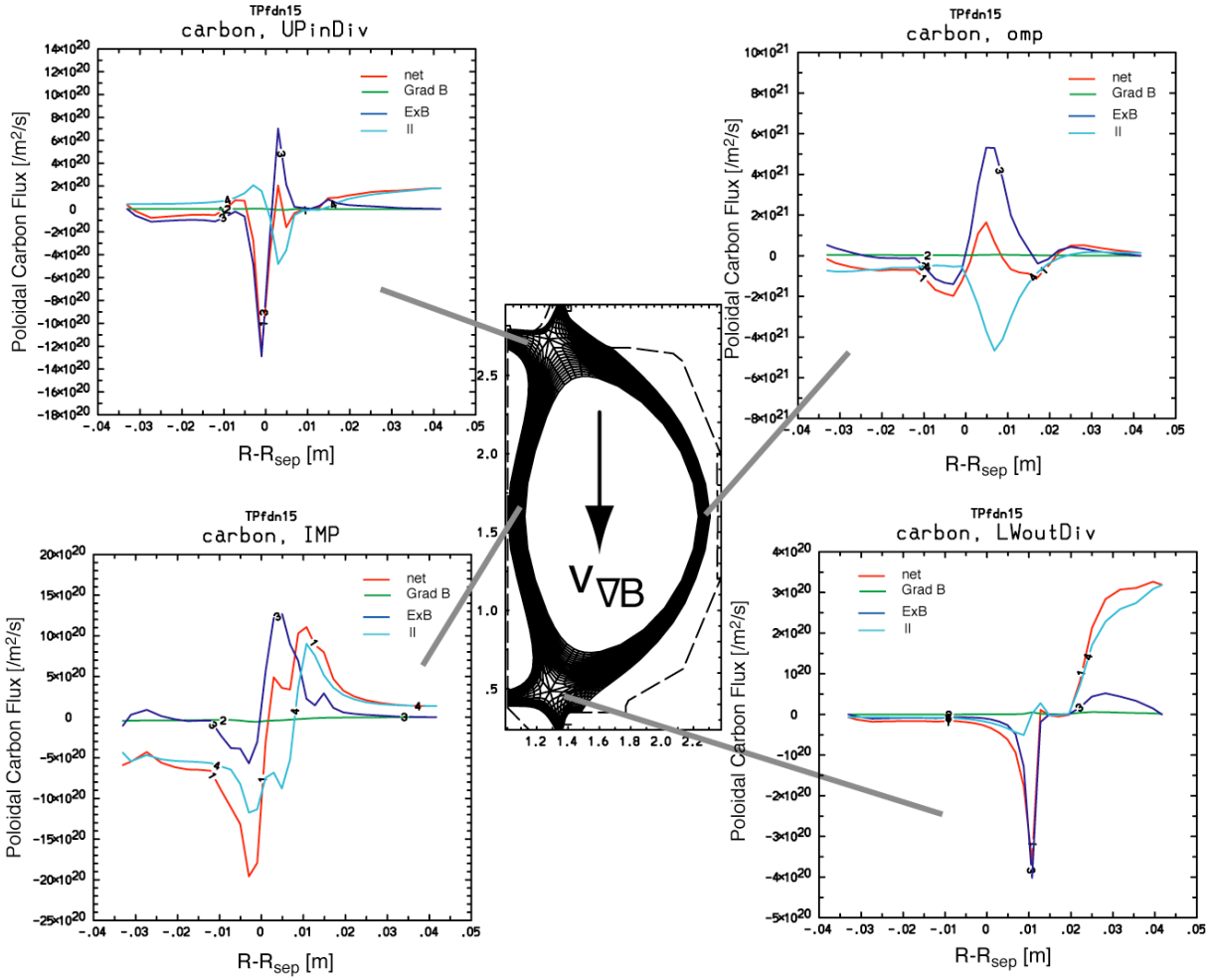
TPfdn15
carbon, UPinDiv
net
Grad B
ExB
II
Poloidal Carbon Flux [/m²/s]
R-Rsep [m]
TPfdn15
carbon, omp
net
Grad B
ExB
II
Poloidal Carbon Flux [/m²/s]
R-Rsep [m]
TPfdn15
carbon, IMP
net
Grad B
ExB
II
Poloidal Carbon Flux [/m²/s]
R-Rsep [m]
TPfdn15
carbon, LWoutDiv
net
Grad B
ExB
II
Poloidal Carbon Flux [/m²/s]
R-Rsep [m]
V∇B

Fig. 12

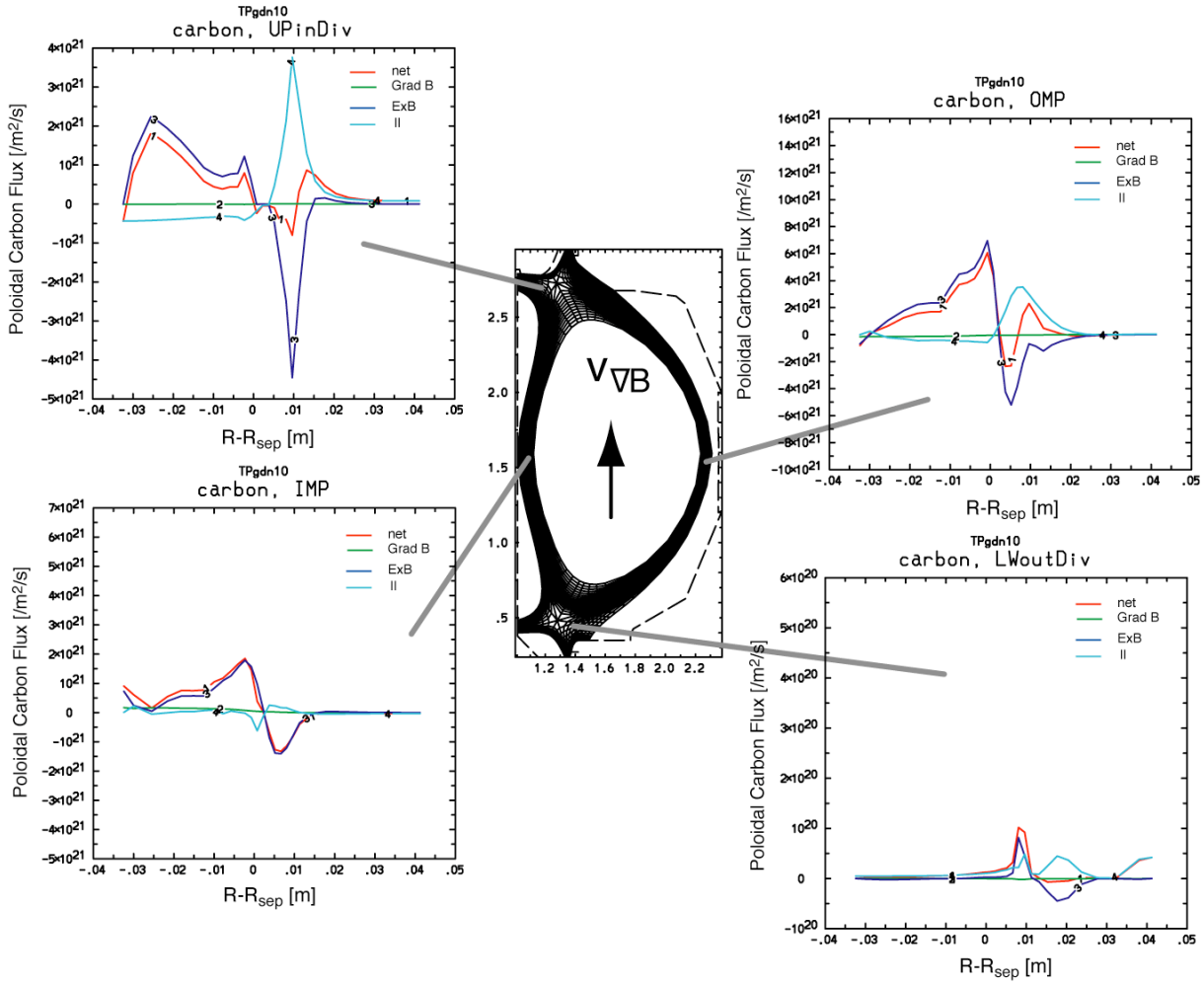
TPgdn10
carbon, UPinDiv
net
Grad B
ExB
II
Poloidal Carbon Flux [/m²/s]
R-Rsep [m]
TPgdn10
carbon, OMP
TPgdn10
carbon, IMP
TPgdn10
carbon, LWoutDiv
V∇B

Fig 13

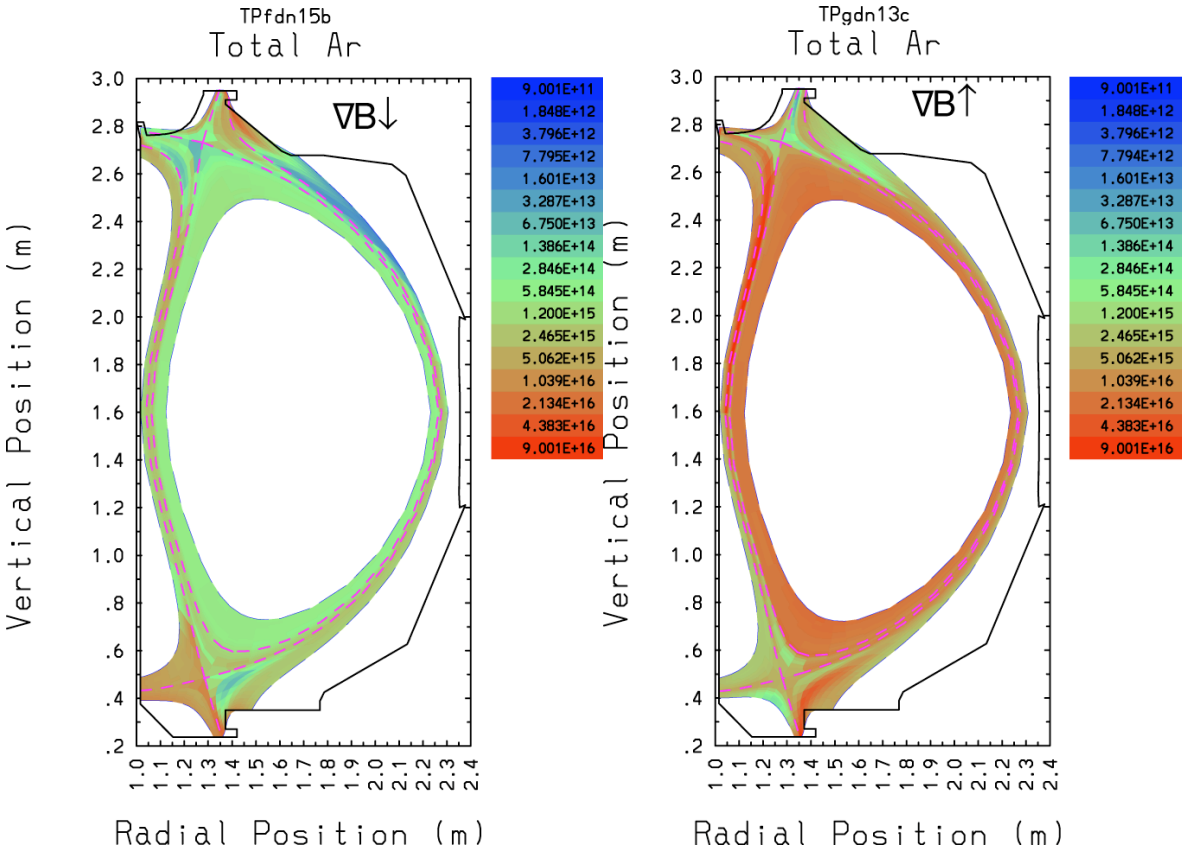
TPfdn15b
Total Ar
∇B↓
TPgdn13c
Total Ar
∇B↑
9.001E+11
1.848E+12
3.796E+12
7.795E+12
1.601E+13
3.287E+13
6.750E+13
1.386E+14
2.846E+14
5.845E+14
1.200E+15
2.465E+15
5.062E+15
1.039E+16
2.134E+16
4.383E+16
9.001E+16
Vertical Position (m)
Radial Position (m)

Fig 14